Factors Governing Cellular Convection in Orographic Precipitation

DANIEL J. KIRSHBAUM AND DALE R. DURRAN

Department of Atmospheric Sciences, University of Washington, Seattle, Washington

ABSTRACT

The development of shallow cellular convection in warm orographic clouds is investigated through idealized numerical simulations of moist flow over topography using a cloud-resolving numerical model. Buoyant instability, a necessary element for moist convection, is found to be diagnosed most accurately through analysis of the moist Brunt–Väisälä frequency (N_m) rather than the vertical profile of θ_e. In statically unstable orographic clouds ($N_m^2 < 0$), additional environmental and terrain-related factors are shown to have major effects on the amount of cellularity that occurs in 2D simulations. One of these factors, the basic-state wind shear, may suppress convection in 2D yet allow for longitudinal convective roll circulations in 3D. The presence of convective structures within an orographic cloud substantially enhanced the maximum rainfall rates, precipitation efficiencies, and precipitation accumulations in all simulations.

1. Introduction

It is widely known that terrain-induced ascent can cause cloudiness and precipitation in the vicinity of mountains and hills. As with all rainstorms, one may attempt to classify orographic precipitation events as either stratiform or convective based on the static stability and structure of the cloudy regions. The subject of stratiform orographic rainfall was investigated by Douglas and Glasspoole (1947), who noted that orographic rains in the British Isles were commonly characterized by conditionally stable upstream sounding profiles, suggesting that smooth, stable ascent over mountains was a primary mechanism for orographic precipitation. This stable ascent hypothesis was also studied by, among others, Fraser et al. (1973) and Hobbs et al. (1973), who calculated the growth and fallout of precipitation using a model for stably stratified flow over the Cascade mountain range. Convective orographic rainfall, on the other hand, involves the presence of buoyant instability in the orographic cloud. As discussed by Banta (1990), one form of moist instability termed ''latent'' instability is characterized by the existence of convective available potential energy (CAPE) in the orographically modified flow. As with conditionally unstable flow over flat terrain, air parcels lifted to the level of free convection in a latently unstable atmosphere can develop into deep convective storms. This type of instability was present in the Big Thompson flash-flood

Corresponding author address: Daniel J. Kirshbaum, Department of Atmospheric Sciences, University of Washington, Box 351640, Seattle, WA 98195-1640.
E-mail: dank@atmos.washington.edu

of 1976 (Caraceña et al. 1979), and in the atmospheric profiles considered by Chu and Lin (2000), who used two-dimensional (2D) numerical simulations to classify deep convective orographic rain events into various regimes based on the moist Froude number.

Not all orographic precipitation, however, can easily be classified as either purely stratiform or convective. Smith (1982) suggested that some shallow embedded convection may be required in many nominally stratiform events in order to produce the high rainfall accumulations that frequently are observed. The likelihood of embedded convection developing within orographic clouds is commonly determined by assessing the potential instability (PI) of the upstream layer that will be lifted to saturation over the mountain (e.g., Banta 1990). Browning et al. (1974), for example, cited the importance of PI in multiple upstream layers in initiating the seeder–feeder process and enhancing rainfall over the Welsh hills. Other examples include Parsons and Hobbs (1983), who investigated the contribution of convection, generated in potentially unstable layers, to the seeder–feeder process in a study of landfalling Pacific midlatitude cyclones, and Grossman and Durran (1984), who noted the presence of PI in an analysis of deep monsoon convection over the eastern Arabian Sea forced by the western Ghat Mountains. In the following, we will critically assess the utility of PI as a predictor for the development of cellular convection in relatively shallow orographic cap clouds.

Although moist instability is a necessary element for the formation of embedded cells within an orographic cloud, it is not the only factor that regulates this convective development. Additional subtle factors can com-

pletely inhibit or profoundly modulate the cellularity of an orographic cloud. One such factor, environmental wind shear, was shown by Asai (1964) and Hill (1968) to be capable of suppressing the growth of infinitessimal perturbations in statically unstable 2D Boussinesq flow. This study will investigate the effect of wind shear, as well as other factors including the residence time of air parcels in the cloud and the depth of the cloud itself, on the degree of cellular development in orographic rainclouds.

The importance of cellular convection in orographic rain events depends largely on the impact such cellularity has on precipitation intensity, precipitation efficiency, and total rainfall accumulation. Although cellular structures within orographic clouds generate stronger updrafts that increase hydrometeor growth through collection and produce locally higher precipitation rates, the increase in precipitation from the updrafts is potentially compensated by decreased precipitation in the downdrafts on the flanks of each cell. There appear to be only a few studies that have investigated the net result of these competing effects on the total area-averaged precipitation and the precipitation efficiency of orographic storms. Elliott and Hovind (1964) estimated the precipitation efficiencies of rain clouds over the Sierra Nevadas with the aid of a hydraulic airflow model and found that conditionally unstable clouds had slightly higher efficiencies (26%–28%) than conditionally stable clouds (17%–25%). Dirks (1973) calculated precipitation efficiencies directly using aircraft data collected over mountains in Wyoming and found efficiencies between 25% and 80% for convectively unstable events. These studies, while indicating that some increase in precipitation efficiency may be associated with orographic convection, do not conclusively show that convection has a major impact on the efficiency or the total precipitation produced by orographic rain events. In this study, the quantitative impact of shallow cellular convection on these precipitation metrics will be further investigated through numerical simulation.

Our analysis of orographic convection will be performed using a cloud-resolving numerical model, which is discussed in the next section. A thorough look at the diagnosis of moist stability within a 2D orographic cloud, and the effects of stability upon the resulting precipitation, will be provided in section 3. Other factors beyond moist stability that regulate the development of orographic convection in an unstable 2D cap cloud will be isolated and analyzed in section 4. The difference between 2D and 3D convective structures in shallow orographic cap clouds will be examined in section 5. Section 6 contains the conclusions.

2. Numerical model

The numerical model used for this analysis is based on Durran and Klemp (1983) and Epifanio and Durran (2001). This model is nonlinear, nonhydrostatic, fully compressible, inviscid, and uses a terrain-following coordinate system. A flux-limited advection scheme (LeVeque 1996) is applied to the potential temperature and moisture fields to reduce spurious overshoots caused by steep spatial gradients. The subgrid-scale turbulence formulation is based on Lilly (1962), and warm-rain microphysics are included through a Kessler parameterization. Ice microphysics are neglected for simplicity and because the cloud tops in most of the simulations considered in this paper barely extend to the freezing level. Simulations will be performed in both 2D and 3D.

For the 2D simulations, Δt is set at 4 s and the spatial resolution is set at $\Delta x = 500$ m and $\Delta z = 100$ m. The size of the computational domain is $L_x = 675$ km in the horizontal and $L_z = 10$ km in the vertical, and the mountain profile, which is centered at $x_0 = 450$ km, is given by

$$h(x) = \begin{cases} \dfrac{h_0}{16}\left[1 + \cos\left(\pi\dfrac{x - x_0}{4\alpha}\right)\right]^4: & |x - x_0| < 4a \\ 0: & |x - x_0| > 4a, \end{cases} \tag{1}$$

where h_0 is the peak mountain height and a is the horizontal half-width.

Three-dimensional simulations of two different types are performed; the first uses a y-periodic quasi-2D ridge and the other uses a finite-length isolated ridge. The numerical parameters for the quasi-2D ridge simulation are similar to those in the 2D simulations, with $\Delta x = \Delta y = 500$ m, $\Delta z = 100$ m, $\Delta t = 4$ s, $L_x = 675$ km, and $L_z = 10$ km, along with $L_y = 20$ km. The terrain in the quasi-2D case is independent of y and determined by (1) with $x_0 = 450$ km. The boundaries are periodic with respect to the y-coordinate, thereby representing an infinitely long barrier.

For the finite-length-ridge simulation, three-level, two-way grid nesting has been employed to reduce computational expense. The spatial and temporal resolution on the finest mesh is the same as in the other simulations, with $\Delta x = \Delta y = 500$ m, $\Delta z = 100$ m, and $\Delta t = 4$ s. The horizontal grid spacing and time step increase to $\Delta x = \Delta y = 1500$ m and $\Delta t = 12$ s on the intermediate mesh and $\Delta x = \Delta y = 4500$ m and $\Delta t = 36$ s on the coarsest mesh. The mountain profile for the isolated ridge simulation has the form

$$h(x, y) = \begin{cases} \dfrac{h_0}{16}[1 + \cos(\pi r)]^4: & r \leq 1 \\ 0: & \text{otherwise}, \end{cases} \tag{2}$$
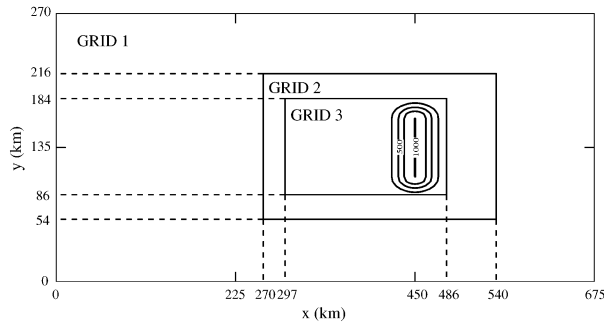
where

FIG. 1. Numerical domain for the isolated-ridge simulation showing the grid nesting and contours of the topography at 250-m intervals.

$$
r^2 = \begin{cases}
\left(\dfrac{x - x_0}{4a}\right)^2 + \left(\dfrac{|y - y_0| - B}{4b}\right)^2: & |y - y_0| > B \\[2em]
\left(\dfrac{x - x_0}{4a}\right)^2: & \text{otherwise.}
\end{cases}
$$

(3)

Figure 1 illustrates the grid configurations and terrain profile for the finite-length 3D ridge simulations, where $h_0 = 1$ km, $B = 30$ km, $a = 20$ km, $b = 10$ km, $x_0 = 450$ km, and $y_0 = 135$ km.

To initiate convective motions within the statically unstable regions produced by the moist orographic flow, random noise of small amplitude is added to the initial thermal fields of all the simulations. This noise field is created by assigning a uniformly distributed random number to each thermodynamic gridpoint, filtering these values by a single application of a diffusion operator along each coordinate axis to remove all forcing at 2Δ, and then scaling the field to have a 0.1 K root-mean-squared (rms) amplitude. In addition to seeding convection in unstable areas, these thermal inhomogeneities generate gravity waves in stable regions, which propagate through the upper and lateral boundaries of the domain, gradually dissipating much of the small-scale energy contained in the initial noise field. The simulations are, therefore, terminated after 4 h, at which time the amplitude of the thermal noise has been reduced to about 50% of its initial value.

3. Moist stability

a. Using θ_e to diagnose moist stability

When sufficiently moist lower-level air is incident upon a mountain, the forced ascent upwind of the mountain peak can cause an entire layer of the atmosphere to saturate. In such an orographic cloud, it is commonly assumed that the basic distinction between cumuliform or stratiform cloud habit can be predicted by checking for potential instability in the upstream atmospheric profile (e.g., Banta 1990). The presence of potential instability throughout a layer is conventionally determined

by looking at the sign of $d\theta_e/dz$, where θ_e is the equivalent potential temperature. A negative value of $d\theta_e/dz$ in a layer of an upstream sounding corresponds to a *potentially unstable* situation, while positive values of $d\theta_e/dz$ correspond to *potentially stable* situations. The existence of potential instability has been widely accepted as a necessary and sufficient condition for a saturated atmosphere to be statically unstable (e.g., Bryan and Fritsch 2000; Glickman 2000).

Various expressions for θ_e have been presented in the literature. Here, we follow Emanuel (1994), whose expression for the equivalent potential temperature,

$$
\theta_e = T\left(\frac{p_0}{p_d}\right)^{R_d/(c_p + c_l q_w)} \left(\frac{q_v}{q_s}\right)^{-q_v R_v/(c_p + c_l q_w)} \exp\left[\frac{Lq_v}{(c_p + c_l q_w)T}\right],
$$

(4)

is conserved for reversible moist adiabatic processes. In the preceding, T is the temperature, p_d is the pressure of the dry air, p_0 is a constant reference pressure, c_p and c_l are the specific heats at constant pressure of dry air and liquid water, R_d and R_v are the ideal gas constants for dry air and water vapor, L is the latent heat of condensation of water, q_v is the mixing ratio of water vapor, q_s the saturation mixing ratio, and q_w the total water mixing ratio.[1]

A representative example of the difference between potentially unstable and stable orographic precipitation may be obtained from data collected during intensive observing periods (IOPs) 3 and 8 of the Mesoscale Alpine Programme (MAP; Bougeault et al. 2001; Houze 2001). Figure 2a shows the 1647 UTC Milan sounding on 25 September 1999 from IOP3, while that in Fig. 2b is the 1105 UTC Milan sounding on 21 October 1999 from IOP8. In IOP3 the surface temperature at Milan was 297 K and there was a layer of relatively low static stability from the surface up to an inversion at about 550 mb, while in IOP8 the surface temperature was lower (279 K) and there was relatively high stability at all levels. The corresponding profiles of θ_e shown in Fig. 2c indicate a layer of negative $d\theta_e/dz$ and potential instability from the surface up to 4.6 km in IOP3, while IOP8 is potentially stable with positive values of $d\theta_e/dz$ at all levels. To capture the important features of these MAP soundings while filtering out extraneous information that may serve to complicate the analysis of our subsequent numerical simulations, smoothed versions of the two soundings from Fig. 2 have been created, and are shown in Fig. 3. Figures 3a and 3b show the respective skew-T plots for the smoothed IOP3 and IOP8 soundings, and Fig. 3c shows the θ_e profiles of the two smoothed soundings overlaid on the actual MAP profiles. This figure shows that the smoothed soundings maintain essentially the same layered structures and

---

[1] As $q_v \to 0$ (with $q_l = q_\tau = 0$), L'Hôpital's rule may be used to show that $\ln[(q_v/q_s)^{-q_v R_v/(c_p + c_l q_w)}] \to 0$, and therefore that θ_e reduces to the dry potential temperature θ.
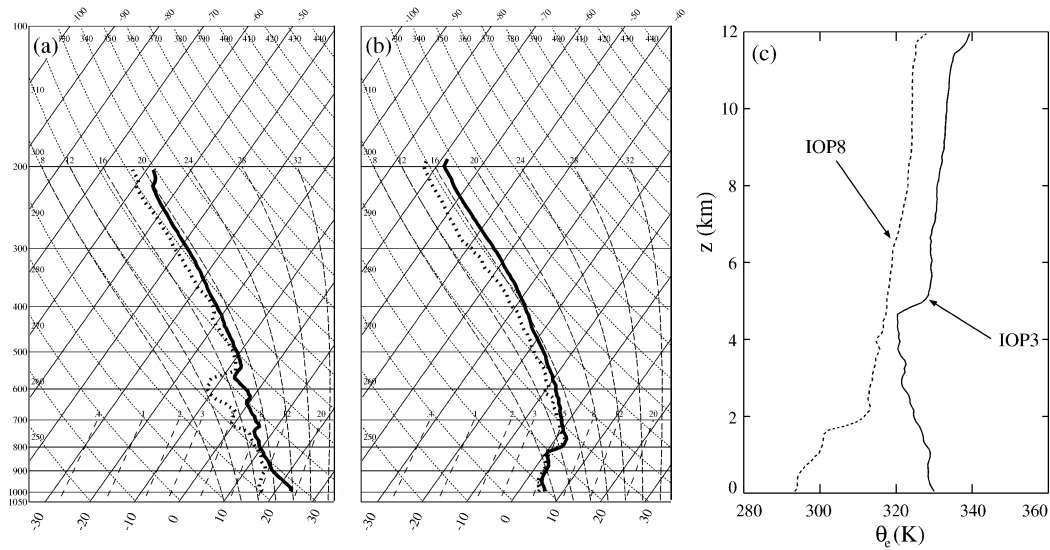
FIG. 2. Comparison of observed skew-T profiles for (a) IOP3 and (b) IOP8; (c) θ_e profiles for both cases.

lower-level θ_e profiles as the observed soundings; the only significant differences are above 9 km, where the smoothed soundings are more stable.

The smoothed IOP3 and IOP8 sounding profiles are used to define the thermodynamic structures in a pair of otherwise completely idealized simulations of flow over 2D topography. The upstream wind speed U in these simulations is a uniform 15 m s^{-1} and the terrain profile is given by (1) with $a = 20$ km and $h_0 = 1$ km. Neither the wind nor the terrain profile are particularly representative of the actual events observed during MAP. The smoothed IOP3 and IOP8 soundings are used in these simulations not in an attempt to model the actual MAP events, but rather to ensure that the moist ther-

modynamic structures in our simulations are representative of those associated with midlatitude orographic precipitation. The cloud liquid water (q_c) fields after 2 h ($t = 7200$ s) from these two simulations (IOP3-control and IOP8) are shown in Figs. 4a and 4b. The IOP3-control simulation (Fig. 4a) has well-developed cellular structures with regions of comparatively high q_c in the updrafts and low q_c in the downdrafts, while the IOP8 simulation (Fig. 4b) produces a stable cap cloud without embedded cells. The enhanced q_c and vertical velocities contained in the cellular updrafts of the IOP3-control simulation also generate much larger surface rainfall rates than those in IOP8, as may be seen by comparing the IOP3-control and IOP8 entries in Table 1.
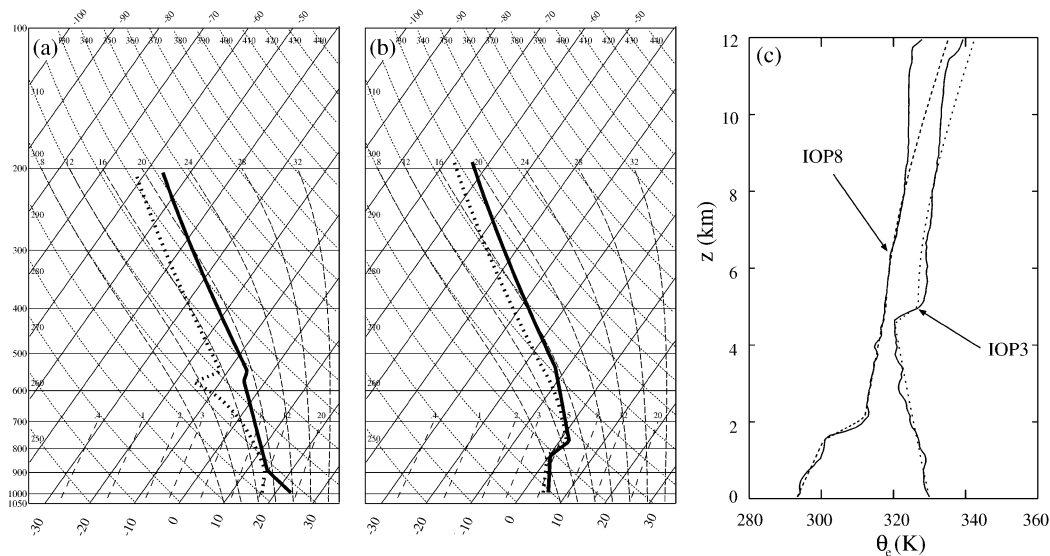

FIG. 3. Comparison of smoothed thermodynamic profiles for (a) IOP3 and (b) IOP8; (c) θ_e profiles for observed (solid) and smoothed (dashed) cases.
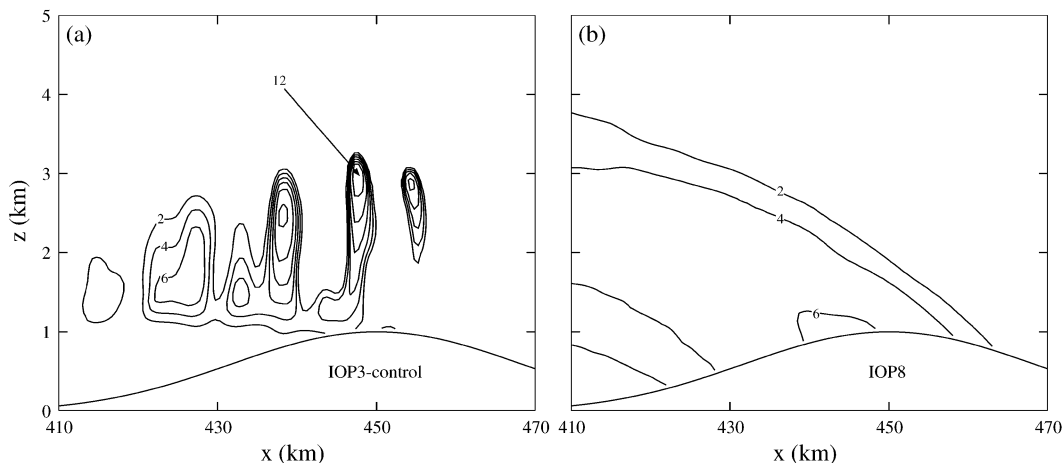
FIG. 4. Cloud liquid water (q_c) at 7200 s for (a) IOP3-control and (b) IOP8 simulations. Contour labels are multiplied by 10^{-4}.

Before continuing the discussion of rainfall in the IOP3-control and IOP8 simulations, we pause to give more details about the information provided in Table 1, which compares four quantities characterizing precipitation generated in the orographic cap clouds of the various simulations described throughout this paper. The first quantity, R_{max}, corresponds to the maximum rainfall rate below the cap cloud[2] during the interval $0 \leq t \leq 14\,400$ s. The next two quantities, $(E_{cloud})_{avg}$ and E_{flow}, are different measures of precipitation efficiency: E_{cloud}, the more commonly used of these two precipitation-efficiency metrics, is defined as the instantaneous ratio of the rainfall rate at the surface to the volume-integrated rate of cloud liquid water formation (Elliott and Hovind 1964; Rogers and Yau 1989); E_{cloud} indicates the ability of the cloud to convert condensed water into surface rainfall—its average value inside the cap-cloud region over the duration of the simulation ($0 \leq t \leq 14\,400$ s) is given in Table 1 and denoted by $(E_{cloud})_{avg}$. The second metric, E_{flow}, is the ratio of the accumulated rainfall at the surface to the time-integrated mass flux of moisture into the cap-cloud region, and is indicative of the ability of the cross-barrier flow to extract precipitation from the upstream air. Because E_{flow} is a cumulative rather than an instantaneous quantity, the values of E_{flow} given in Table 1 are for 14 400 s. The final quantity shown in the table is P_{avg}, the accumulated precipitation at 14 400 s averaged over the lower boundary of the cap-cloud region.

Returning to the discussion of rainfall intensity generated by the IOP3-control and IOP8 simulations, Table 1 shows that R_{max} for the IOP3-control case (35.2 mm h^{-1}) is over 10 times greater than that produced by the IOP8 case (2.2 mm h^{-1}). The table also shows that both measures of precipitation efficiency [$(E_{cloud})_{avg}$ and E_{flow}], as well as P_{avg}, are much greater for the IOP3-

control simulation than for the IOP8 simulation. These results indicate that the convective IOP3-control simulation produces precipitation of greater intensity, efficiency, and accumulation than the stable IOP8 simulation. The profound differences in precipitation output between the two simulations can be attributed, at least in part, to the ability of cellular updrafts in the IOP3-control simulation to facilitate hydrometeor growth in the cloud and produce precipitation-sized droplets more rapidly. However, the inability of the warm-rain microphysical scheme employed for these simulations to represent ice aggregation processes may also suppress the rainfall totals in the IOP8 case, which was cold enough (Fig. 3b) and contained a sufficiently extensive cloud shield (visible in Fig. 4b) to produce broad regions of glaciation.

b. Looking beyond the θ_e profile

Although in the preceding example it is possible to adequately diagnose the potential for cellularity simply by analyzing the vertical profile of θ_e, more information is generally required to determine the cloud habit. One

---

[2] For the calculations in Table 1, the cap cloud is defined as all clouds in the region $0 \leq x \leq 470$ km and $0 \leq z \leq 5$ km.

TABLE 1. Comparison of precipitation quantities for various simulations: R_{max} is maximum surface rain rate over $0 \leq t \leq 14\,400$ s; $(E_{cloud})_{avg}$ is average cloud precipitation efficiency over $0 \leq t \leq 14\,400$ s; E_{flow} is percentage of total inflow moisture converted to precipitation through $t = 14\,400$ s; P_{avg} is total precipitation averaged over the surface of the domain through $t = 14\,400$ s.

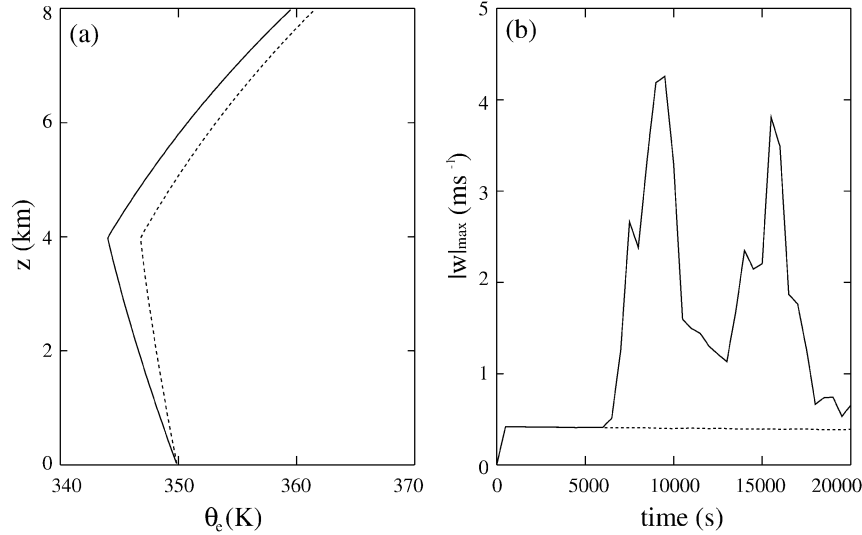| Simulation	R_{max} (mm h^{-1})	$(E_{cloud})_{avg}$ (%)	E_{flow} (%)	P_{avg} (mm)
IOP3-control	35.2	42.6	4.2	0.69
IOP8	2.2	19.6	2.6	0.26
IOP3-narrow	8.4	27.5	1.5	0.25
IOP3-shal	23.6	38.0	2.5	0.40
IOP3-deep	61.5	47.1	6.1	1.04
IOP3-shear	15.0	34.3	1.9	0.40
IOP3-shear-q2D	68.1	45.9	3.4	0.72

FIG. 5. Comparison of two simulations with different lower-level moist stabilities: $N_m^2 = -4 \times 10^{-6}$ s^{-2} (solid lines) and $N_m^2 = 4 \times 10^{-6}$ s^{-2} (dashed lines); (a) θ_e profile, (b) maximum absolute vertical velocity $|w|$ as a function of time.

reason additional information is necessary is that, as will be considered in section 4, the development of embedded cells in orographic clouds is affected by other parameters not directly related to the potential stability of the upstream flow. A second reason is that the vertical profile of θ_e, by itself, is inadequate to completely define the thermodynamic structure of the flow because the static stability of saturated air is determined by the moist Brunt–Väisälä frequency rather than the sign of $d\theta_e/dz$. As noted by Durran and Klemp (1982) and Emanuel (1994), the precise condition for static instability to infinitessimal vertical displacements in a saturated layer is not $d\theta_e/dz < 0$, but rather that the moist Brunt–Väisälä frequency be imaginary. The moist Brunt–Väisälä frequency N_m, as derived by Lalas and Einaudi (1974), may be written

$$N_m^2 = \frac{g}{T}\left(\frac{dT}{dz} + \Gamma_m\right)\left(1 + \frac{Lq_s}{R_d T}\right) - \frac{g}{1 + q_w}\frac{dq_w}{dz}, \quad (5)$$

where Γ_m is the moist adiabatic lapse rate. Equivalent expressions for N_m^2 in terms of moist conservative variables have been derived by Durran and Klemp (1982)[3] and Emanuel (1994). From Emanuel's expression for N_m^2,

$$N_m^2 = \frac{1}{1 + q_w}\left\{\Gamma_m\frac{d}{dz}[(c_p + c_l q_w)\ln\theta_e]\right.$$

$$\left. - [c_l\Gamma_m\ln(T) + g]\frac{dq_w}{dz}\right\}, \quad (6)$$

[3] Equation (21) of Durran and Klemp (1982) erroneously omits the term $-g/1 + q_w\{(\Gamma_m/\Gamma_d)c_l/c_p \ln(T/T_0)dq_w/dz\}$.

it is clear that the sign of N_m^2 is not determined solely by the sign of $d\theta_e/dz$. In particular, the vertical gradient of q_w also plays a role in determining the moist static stability.

A simple example contrasting the accuracy with which N_m^2 and $d\theta_e/dz$ may be used to diagnose moist static stability is provided by comparing two simulations with slightly different horizontally uniform thermodynamic profiles. Cloudy layers in both simulations are specified such that $q_c = 1 \times 10^{-4}$ from the surface to 4 km and $q_c = 0$ in an unsaturated region between 4 km and the top of the domain at 8 km. The sign of N_m^2 in the cloudy layer differs between the two simulations—in one case $N_m^2 = 4 \times 10^{-6}$ s^{-2} and in the other $N_m^2 = -4 \times 10^{-6}$ s^{-2}. Although the sign of N_m^2 is different for the two simulations, both cases have negative $d\theta_e/dz$ inside the cloud, as can be seen from the θ_e profiles shown in Fig. 5a. Throughout the upper, unsaturated half of the domain, $N^2 = 2.2 \times 10^{-4}$ s^{-2}, and the relative humidity decreases linearly with height to 50% at 8 km for both simulations. Each air mass is advected at $U = 10$ m s^{-1} over a roughened horizontal surface to determine whether the cloud is unstable to small surface-induced perturbations. The width of the domain is 40 km and resolution is set at $\Delta x = 100$ m, $\Delta z = 50$ m, and $\Delta t = 1$ s, and filtered random noise with an rms amplitude of 5 m (created in an identical fashion to the thermal noise field discussed in section 2) has been added to the otherwise flat topography. The lateral boundary conditions are periodic to allow for infinite residence times for air parcels in the saturated region.

Figure 5b shows a plot of maximum vertical velocity as a function of time for these two simulations. The
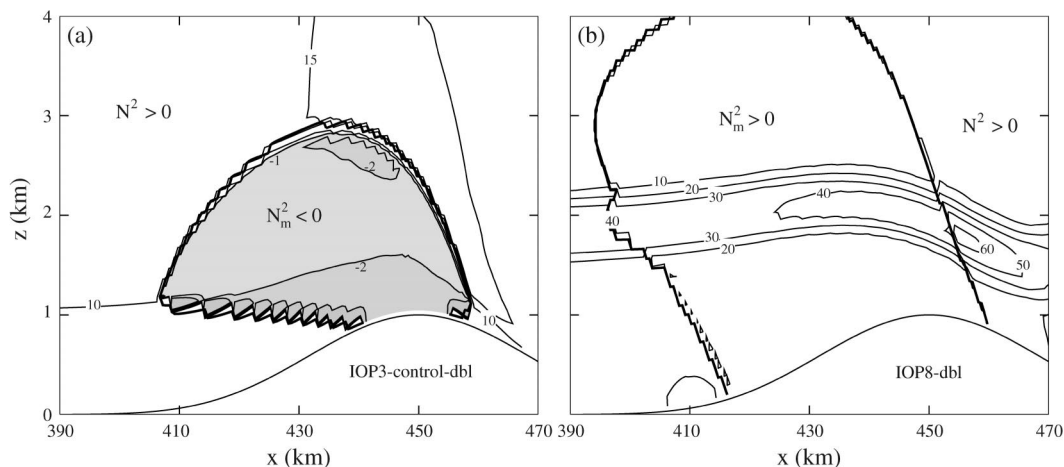
FIG. 6. Comparison of the square of the Brunt–Väisälä frequency at 1200 s for (a) IOP3-control-dbl and (b) IOP8-dbl simulations; N_m^2 is plotted inside cloud, N^2 outside. Shaded areas correspond to negative values. Cloud outline given by thick solid line. Contour labels are multiplied by 10^{-5} s^{-2}.

simulation with $N_m^2 < 0$ produces maximum vertical velocities that amplify rapidly after 7000 s and exceed 4 m s^{-1} by 9000 s, whereas the simulation with $N_m^2 > 0$ maintains a nearly steady maximum vertical velocity of around 0.4 m s^{-1}. These results reflect the fact that convective overturning and episodic development of rapidly amplifying cells has been triggered in the simulation with $N_m^2 < 0$, while the simulation with $N_m^2 > 0$ only develops stable gravity waves whose amplitudes are governed by the strength of the surface-induced perturbations. In this example N_m^2, rather than $d\theta_e/dz$, must be used to correctly predict the development of moist instability.

Looking back at the example in section 3a, the difference in cellularity between the IOP3-control and IOP8 simulations apparent in Fig. 4 can easily be explained by differences in N_m between the two cases. To clearly show the differences in the nominal stabilities of the two simulations without the presence of irregular thermal perturbations and cellular structures, Fig. 6 shows the fields of Brunt–Väisälä frequency at $t = 1200$ s for two simulations (IOP3-control-dbl and IOP8-dbl), which are identical to IOP3-control and IOP8, except they are performed in double precision without the presence of thermal perturbations. In saturated regions N_m^2 is plotted, N^2 is shown in unsaturated areas. The removal of thermal perturbations and the use of double precision to minimize truncation error in the IOP3-control dbl and IOP8-dbl simulations reduce the amplitudes of all small-scale perturbations available to initiate convection, so that the cap cloud remains laminar in both cases. Inside the cap cloud of the IOP3-control-dbl simulation N_m^2 is negative, indicating nominally statically unstable conditions, while IOP8-dbl has positive Brunt–Väisälä frequencies and stable flow throughout the domain. When thermal perturbations are added to the flow, these large differences in static stability cause very different behaviors; the IOP3-control case develops organized cel-

lular structures, while the cloud in IOP8 remains laminar (see Fig. 4).

4. Other factors influencing cellularity

The comparisons of section 3 demonstrated the necessity for static instability, as defined by $N_m^2 < 0$, to be present in a cloud for convective cells to develop. In statically unstable clouds such as the upslope cap cloud in the IOP3-control simulation, other factors not directly related to the stability of the flow can also influence the degree of cellularity. In this section we examine the effects of three such factors on the development of cellular convection in orographic precipitation: 1) the residence time of air parcels in the saturated region of the cap cloud, 2) the depth of the saturated unstable layer, and 3) basic-state wind shear. The influence of these factors is shown in Figs. 4 and 7 by the q_c fields at $t = 7200$ s from five simulations (IOP3-control, IOP3-narrow, IOP3-shal, IOP3-deep, and IOP3-shear) having similar levels of moist instability in their cap clouds, but different environmental and terrain-related characteristics that modulate the cellular development within the clouds.

A detailed description and analysis of each these simulations will be presented later in this section; here we provide a brief overview of the basic results. In comparison with the control simulation (Fig. 4a), air flowing over a narrower ridge fails to develop significant cells (Fig. 7a). When the orographic cloud is relatively shallow, the cells are weaker (Fig. 7b) than when the cloud is deep (Fig. 7c). In addition, vertical wind shear inhibits the development of strong cells in 2D (Fig. 7d). The wide variations in cellularity apparent between these five simulations is reflected in the precipitation comparison of Table 1, which shows that the more cellular appearing clouds produce higher rainfall rates, efficiencies, and accumulations.
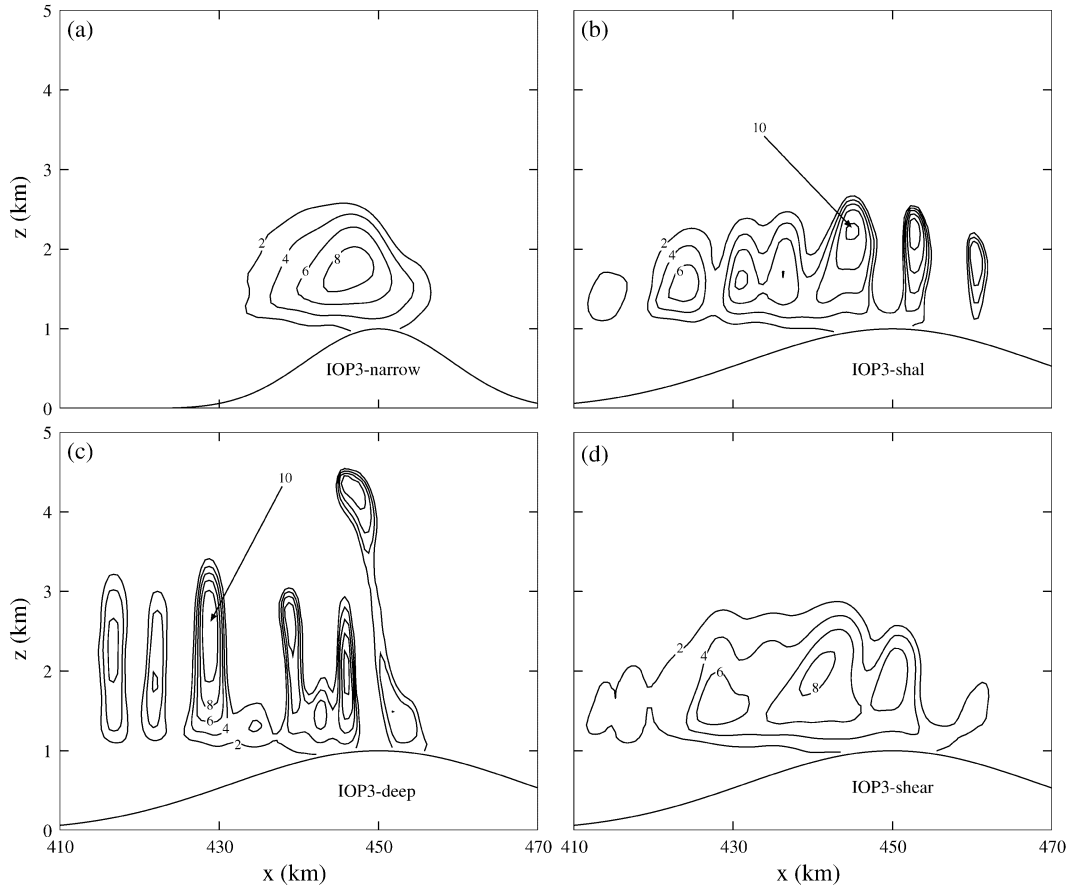
FIG. 7. Comparison of q_c at 7200 s for various 2D simulations. (a) IOP3-narrow, (b) IOP3-shal, (c) IOP3-deep, and (d) IOP3-shear. Contour labels are multiplied by 10^{-4}.

Before addressing the specific factors that affect the amount of cellular development in orographic precipitation events, we first introduce a linear analytical model, which serves as a simple construct for understanding cell growth in statically unstable clouds. The model consists of two layers, the lower of which (layer 1) is bounded by a flat surface and is statically unstable, while the overlying layer (layer 2) is stably stratified and infinitely deep. This two-layer structure provides an idealized representation of more complex flows such as that in the IOP3-control simulation (Fig. 6a), in which a deep layer of statically stable air flows over an unstable cloud region. The following expression for the vertical velocity w_i in each layer can be derived from the 2D linearized Boussinesq system of equations:

$$\left(\frac{\partial}{\partial t} + U_i\frac{\partial}{\partial x}\right)^2\left(\frac{\partial^2 w_i}{\partial x^2} + \frac{\partial^2 w_i}{\partial z^2}\right)$$

$$- \frac{\partial^2 U_i}{\partial z^2}\left(\frac{\partial}{\partial t} + U_i\frac{\partial}{\partial x}\right)\left(\frac{\partial w_i}{\partial x}\right) + N_i^2\frac{\partial^2 w_i}{\partial x^2} = 0, \quad (7)$$

where $U_i(z)$ is the basic-state cross-mountain wind speed, and N_i^2 the Brunt–Väisälä frequency in each lay-

er. Suppose that $U_i(z)$ is constant (U_0) in both layers and that, in the statically unstable lower layer, $N_1 = iN_m$. Imposing the lower boundary condition that $w_1 = 0$ at $z = 0$, solutions in the lower layer exist of the form

$$w_1(x, z, t) = Ae^{\omega t} \sin[k(x - U_0 t)] \sin(m_1 z), \quad (8)$$

where the vertical wavenumber m_1, the horizontal wavenumber k, and the frequency ω satisfy the dispersion relation

$$\omega^2 = \frac{(N_1 k)^2}{k^2 + m_1^2}. \quad (9)$$

The frequency ω can be seen from (8) to represent the growth rate for unstable perturbations; its inverse τ_{buoy} is the e-folding time scale for cellular amplification. Requiring $w \to 0$ as $z \to \infty$, evanescent wave solutions of the form

$$w_2(x, z, t) = Ce^{\omega t} \sin[k(x - U_0 t)]De^{-m_2 z} \quad (10)$$

may exist in the upper layer subject to the dispersion relation
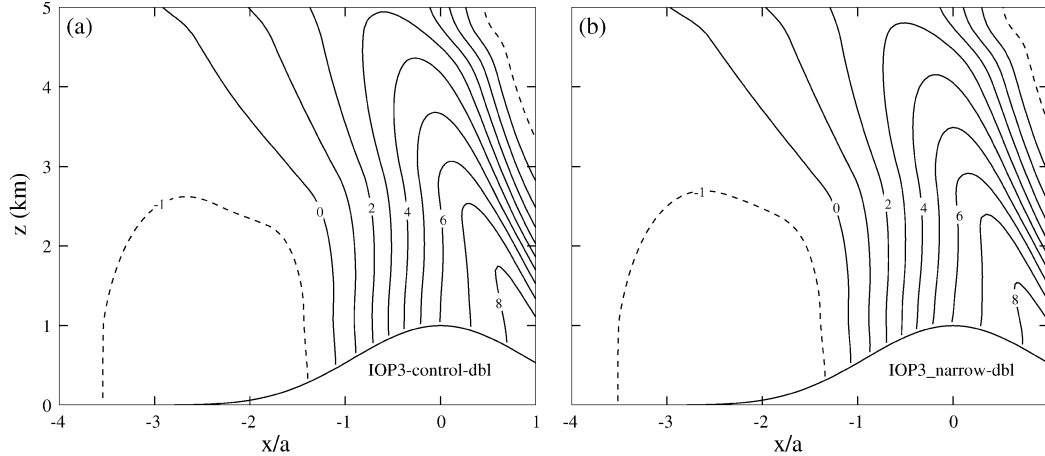
$$\omega^2 = \frac{(N_2 k)^2}{m_2^2 - k^2}, \quad (11)$$

FIG. 8. Horizontal velocity perturbation fields u' at $t = 1.5\tau_{adv}$ for (a) IOP3-control-dbl simulation and (b) IOP3-narrow-dbl simulation. Contour labels are in units of m s^{-1}.

where m_2 is the vertical wavenumber in this layer. Matching w and pressure p at the interface between the two layers at $z = H$, we obtain

$$\tan\left[\frac{kH}{\omega}(N_1^2 - \omega^2)^{1/2}\right] = -\left(\frac{N_1^2 - \omega^2}{N_2^2 + \omega^2}\right)^{1/2}. \quad (12)$$

The e-folding time $\tau_{buoy} = \omega^{-1}$ for cellular amplification may be determined for given values of k, H, N_1, and N_2 from (12).

The e-folding times calculated from the two-layer linear Boussinesq model will be compared with those obtained empirically for the early stage growth of embedded cells within the numerically simulated orographic clouds. The basic state in the two-layer model is, of course, a considerable simplification of that in which cells grow within the parent orographic cloud. Neither the parent cloud nor the velocity field within the cloud are horizontally and vertically uniform, instead both are modulated on the scale of the ridge by mountain-wave-induced perturbations. Nonetheless, as will be seen by applying the two-layer model in the upcoming examples, linear values found using (12) [denoted by $(\tau_{buoy})_L$] generally lie within 15% of experimental e-folding times $[(\tau_{buoy})_E]$ computed by tracking the growth of cells in the numerically simulated clouds. The close agreement between the theoretical model and the empirical data suggests that this linear formulation, with its simple relationships between physical parameters, may be used to understand many of the basic sensitivities of convective cell growth in orographic clouds.

a. Residence time

When a cloud forms on the upwind side of a mountain, air parcels advected by the mean flow will travel through the cloud over a time period determined by the dimensions of the cloud and the velocity of the parcel. The period during which air parcels reside within the cloud is roughly proportional to the advective time scale $\tau_{adv} = a/U$. To determine whether this time period is long enough for moist convective instability to create obvious cellular features in the cloud, it is useful to compare τ_{adv} to τ_{buoy}, the e-folding time scale for moist buoyant instability. Provided that $N_m^2 < 0$, cellular convection is more likely to occur for $\tau_{adv} \gg \tau_{buoy}$ because the air parcels spend enough time inside the unstable cloud to experience many e-folding amplifications.

The effect of in-cloud residence time on cellularity has been investigated by comparing two otherwise identical simulations with different mountain half-widths. The first simulation, corresponding to $a = 20$ km, is the IOP3-control simulation described in section 3a, while the second simulation (IOP3-narrow) has a value of $a = 10$ km. In both of these simulations, the mountain is sufficiently wide so that the basic mountain wave response is hydrostatic, and the horizontal structure of the disturbance scales with a. This correspondence can be most clearly seen by comparing two laminar versions of the control and narrow mountain simulations (IOP3-control-dbl and IOP3-narrow-dbl), which are identical to IOP3-control and IOP3-narrow except that no noise is present in the initial θ fields and all computations are performed in double precision. Since the only perturbations available to initiate the development of cellular overturning arise from roundoff errors in the double-precision calculation, the simulated clouds do not produce significant cells, and the fields from these simulations provide a clean depiction of the orographically disturbed flow in which the cells grow in the IOP3-control and IOP3-narrow simulations. Figure 8 shows that the horizontal perturbation velocities of IOP3-control-dbl and IOP3-narrow-dbl are virtually identical when plotted at identical nondimensional times $t/\tau_{adv} = 1.5$ and displayed with respect to the scaled horizontal axis x/a. Thus, the parent cloud and the environment in which cells grow in
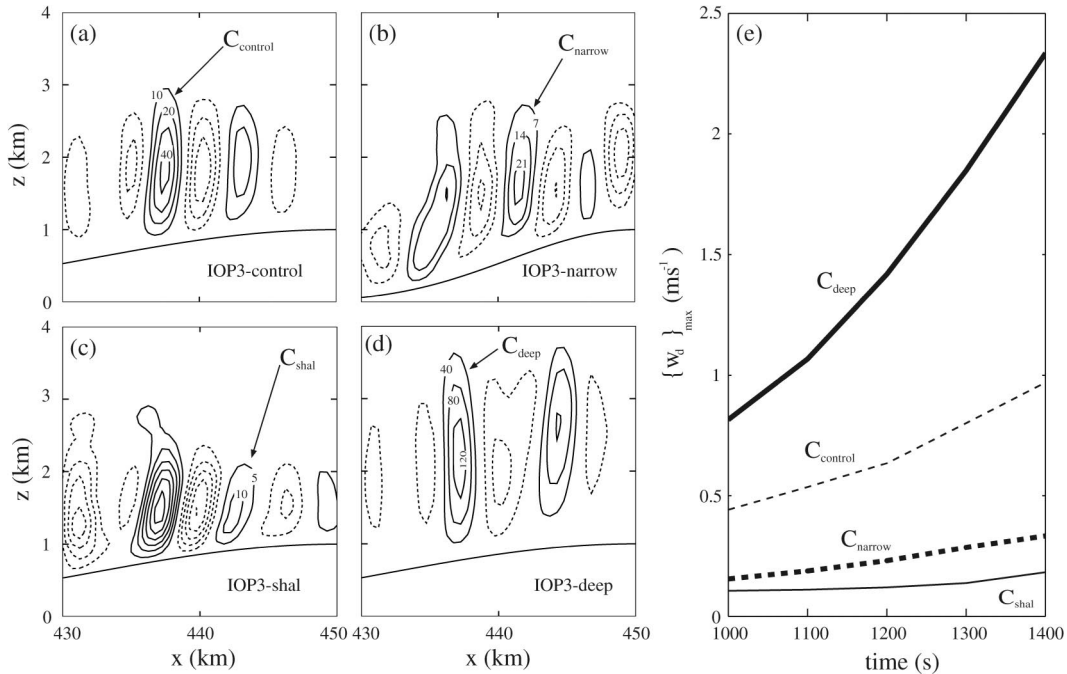
FIG. 9. Comparison of perturbation vertical velocity amplitudes Δw. Contours of Δw at 1200 s for (a) IOP3-control, (b) IOP3-narrow, (c) IOP3-shal, and (d) IOP3-deep. Contour labels are multiplied by 10^{-2} m s^{-1}. (e) Maximum of Δw in updrafts $C_{control}$ (thin dashed line), C_{narrow} (thick dashed line), C_{shal} (thin solid line), and C_{deep} (thick solid line) traveling up the slope for $1000 \leq t \leq 1400$ s.

the control and narrow-mountain simulations are essentially identical except for the difference in horizontal scale and the associated difference in τ_{adv}.

To examine the structure and development of unstable perturbations in the two cases with differing mountain widths, the vertical velocities w of the IOP3-control and IOP3-narrow simulations are now compared with the vertical velocities w_d of the laminar IOP3-control-dbl and IOP3-narrow-dbl simulations, respectively, thus isolating the perturbation velocities within the developing convective eddies. Figures 9a and 9b show the $\Delta w = w - w_d$ fields for the IOP3-control and IOP3-narrow simulations at $t = 1200$ s, indicating that the cellular perturbations in the narrow mountain simulation have similar structure, yet somewhat smaller amplitudes, than those in the IOP3-control case. The maximum vertical velocities in the updrafts labeled $C_{control}$ in Fig. 9a and C_{narrow} in Fig. 9b were diagnosed in a Lagrangian reference frame traveling upslope with the updraft cores between $t = 1000$ and 1400 s and plotted in Fig. 9e. The best-fit e-folding times $(\tau_{buoy})_E$ for the curves shown in Fig. 9e are 509 s and 522 s for the IOP3-control and IOP3-narrow simulations, respectively.

These empirical e-folding times may be compared with those from the two-layer model by substituting representative estimates for N_1, N_2, k, and H into (12). The structure of the static-stability field at $t = 1200$ s in the IOP3-control simulation is shown in Fig. 6a. For both the IOP3-control and IOP3-narrow simulations the

static stabilities within and above the cloud are taken as $N_m = 0.004i$ s^{-1} and $N_2 = 0.012$ s^{-1}, and a value of $H = 1.75$ km is obtained by averaging the depth of the cloud in the vicinity of the cells $C_{control}$ and C_{narrow} over the period $1000 \leq t \leq 1400$ s. The horizontal wavelengths in both simulations are computed by measuring the widths of the updraft cells $C_{control}$ and C_{narrow}, and yield identical estimates of $k = 2\pi/5.7$ km^{-1}. Substituting these values into (12), we obtain linear model estimates of $(\tau_{buoy})_L = 448$ s for both cases. These values are 12% and 14% smaller than the $(\tau_{buoy})_E$ values determined empirically for IOP3-control (509 s) and IOP3-narrow (522 s), indicating reasonably good agreement between the numerical simulations and the simple linear model.

Comparing the q_c fields in the numerical simulations at $t = 7200$ s, Fig. 4a shows well-developed cells in the IOP3-control simulation, while the IOP3-narrow simulation (Fig. 7a) exhibits little to no cellular development. This difference in cellularity appears to be due to the factor-of-2 difference in the residence time over the different mountains, which allows air parcels in the IOP3-control simulation to undergo about twice as many e-folding amplifications ($\tau_{adv}/\tau_{buoy} = 3.0$) as those in the IOP3-narrow simulation ($\tau_{adv}/\tau_{buoy} = 1.5$). Table 1 shows that the difference in cellularity between these two simulations is also reflected in the precipitation, as R_{max}, $(E_{cloud})_{avg}$, E_{flow}, and P_{avg}, are all much larger for the IOP3-control simulation than for IOP3-narrow. In summary, the shorter residence times over the narrow moun-
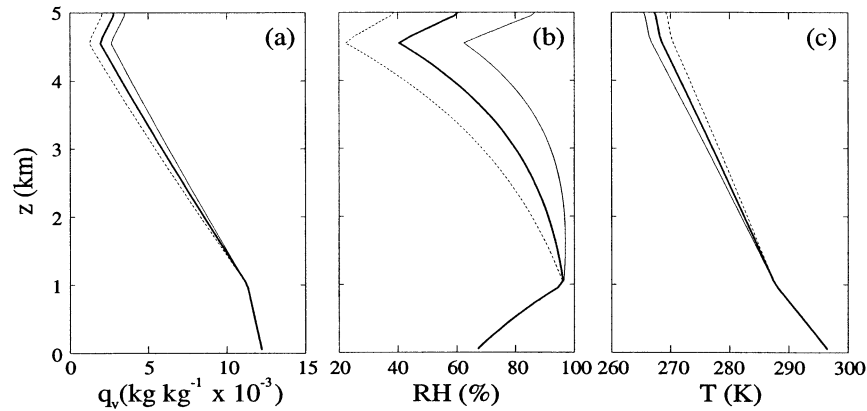
FIG. 10. Profiles for cloud depth comparison. IOP3-shallow given by dotted line, IOP3-control given by thick solid line, IOP3-deep profile given by thin solid line; (a) q_v profiles, (b) relative humidity profiles, and (c) temperature profiles.

tain inhibit cellular convection and thereby reduce the intensity, efficiency, and accumulation of orographic precipitation. The existence of quasi-laminar flow within a statically unstable environment such as that in the IOP3-narrow simulation is not a fundamentally new result; similar behavior has also been documented by Bryan and Fritsch (2000) in a different context (namely in the inflow regions of mesocale convective systems).

b. Cloud depth

To determine the effect of the depth of the parent orographic cloud on the development of embedded cellular convection, consider (9), which may be used to relate the initial growth rate of the cells to their vertical scale. For given values of N_m and k, the growth rate ω is maximized for minimum values of vertical wavenumber m, or equivalently for maximum values of the vertical wavelength λ_z. Since the maximum vertical wavelength of the perturbation in the saturated region increases with the depth of the unstable cloud, deeper clouds are associated with higher growth rates and more rapid cellular development. The same dependence of growth rate on cloud depth is implied via the less transparent mathematical relation (12).

The influence of cloud depth on cellularity is explored using three simulations in which the θ_e profile of the upstream sounding is held constant while the low-level moisture profiles are varied slightly. These small variations in q_v produce three distinct depths in the parent orographic clouds, yet maintain similar moist stabilities inside each cloud. The three simulations are IOP3-control, a shallow-cloud simulation in which the moisture drops off more rapidly with depth (IOP3-shal), and a deep-cloud simulation where the moisture drops off more slowly with depth (IOP3-deep). In order to keep $d\theta_e/dz$ constant as the q_v profile is changed, it is necessary to adjust N^2 slightly. Figure 10 shows a comparison of the q_v, relative humidity, and temperature

profiles for all three simulations. Note that only slight changes in the temperature and moisture fields are necessary to produce the changes in cloud depth. These slight changes in q_v do not produce significant variations in the nominal N_m^2 between the three simulations, which can be most clearly seen by comparing the Brunt–Väisälä frequency fields of thermal-perturbation-free, double-precision versions of the shallow cloud, control, and deep cloud simulations (IOP3-shal-dbl, IOP3-control-dbl, and IOP3-deep-dbl, respectively), which all produce laminar clouds free of small-scale irregularities and convective cells. Figure 11 shows the cloud outlines and contours of the Brunt–Väisälä frequency fields of these three simulations at 1200 s, indicating that the cloud depths at this time range from 1.4 km in the IOP3-shal-dbl case, to 1.8 km in the IOP3-control-dbl case, to 2.8 km in the IOP3-deep-dbl case. This figure also indicates that, in spite of the variations in cloud depth, the different soundings yield similar moist stabilities.

The relationship between cloud depth and the growth rates of unstable perturbations is now examined by comparing linear e-folding times from the two-layer Boussinesq model for the IOP3-shal and IOP3-deep simulations (the IOP3-control case was considered in the previous section). This calculation is again performed by estimating representative values of N_1, N_2, k, and H from the numerically simulated data, then using (12) to obtain the growth rates ω and e-folding times $(\tau_{\mathrm{buoy}})_L$. As in the IOP3-control case, N_m is estimated to be $0.004i$ s^{-1} for both simulations, while N_2 is taken as 0.0125 s^{-1} and 0.011 s^{-1} in the IOP3-shal and IOP3-deep cases, respectively. Estimates for k and H are again determined by subtracting the w_d fields of the laminar simulations (IOP3-shal-dbl and IOP3-deep-dbl) from the w fields of the IOP3-shal and IOP3-deep cases to isolate the cellular perturbations. The cells labeled C_{shal} and C_{deep} in the resulting $\Delta w = w - w_d$ fields of the IOP3-shal (Fig. 9c) and IOP3-deep (Fig. 9d) simulations suggest values of $k = 2\pi/5.5$ s^{-1} for IOP3-shal and $k = 2\pi/6$ km^{-1}
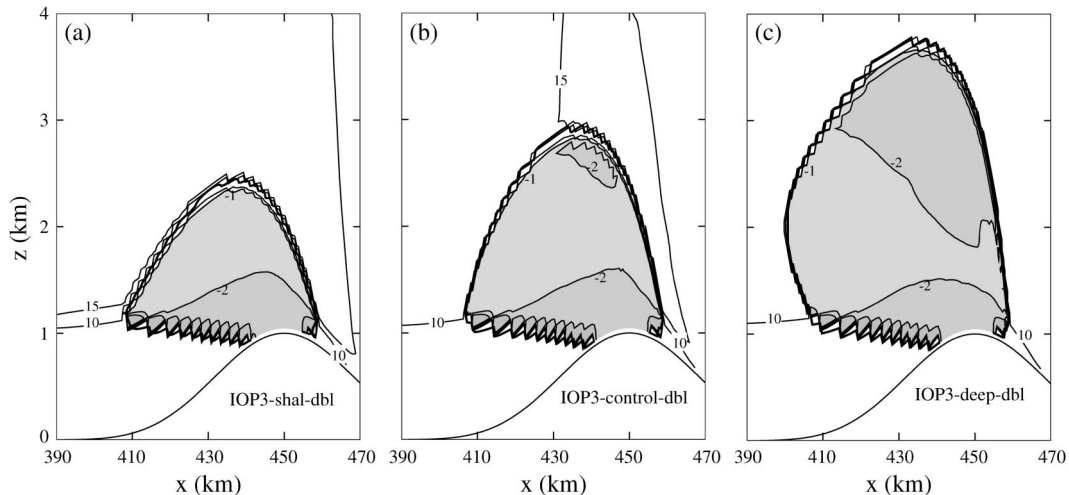
FIG. 11. Cloud outline and static stability fields for cloud depth comparison at 1200 s: (a) IOP3-shal-dbl, (b) IOP3-control-dbl, and (c) IOP3-deep-dbl. Shaded areas indicate regions of negative N^2 or N_m^2. Cloud outline given by thick solid line. Contour labels are multiplied by 10^{-5} s^{-2}.

for IOP3-deep. The average cloud depths over $1000 \leq t \leq 1400$ above these updraft cores are $H = 1.35$ km and 2.6 km in IOP3-shal and IOP3-deep, respectively. These estimates yield $(\tau_{buoy})_L$ values of 528 s and 351 s from (12) for the IOP3-shal and IOP3-deep simulations, which, combined with the previously determined value of 448 s for the IOP3-control case, suggest that perturbation e-folding times are smaller, thus growth rates are larger, as the unstable cloudy layers become progressively deeper.

These differences in perturbation growth rates lead to widely varying degrees of cellularity in the nonlinear simulations. Figure 7c shows that, at $t = 7200$ s, the cloud in the IOP3-shal simulation has undergone only a small amount of cellular development, while cells are clearly apparent in both the IOP3-control simulation (Fig. 7a) and the IOP3-deep case (Fig. 7d). Table 1 indicates that R_{max}, $(E_{cloud})_{avg}$, E_{flow}, and P_{avg} all increase with the depth of the cloud and the degree of cellularity in these simulations.

Note that the shallow, control, and deep cases produce convective cells that are not steady, and comparison of the relative strengths of the cells at a single time can be misleading. For example, there is no single cell representative of the typical strength of cells in the IOP3-deep case at 7200 s. Figure 12, which compares the q_c fields of the IOP3-shal, IOP3-control, and IOP3-deep simulations after 1 h ($t = 3600$ s) and 3 h ($t = 10\,800$ s), shows that, at both of these times, the cloud in the IOP3-deep case (Figs. 12e and 12f, respectively) exhibits stronger cellular development and higher maximum q_c values than at 7200 s (Fig. 7c). In addition, unlike in the comparison at 7200 s, the cells in the IOP3-deep case at 3600 s and 10 800 s are clearly stronger than those in both the IOP3-shal (Figs. 12a and 12b, respectively) and IOP3-control (Figs. 12c and 12d, re-

spectively) simulations. Note also the that the intensity of the convective cells in each simulation decreases somewhat between 3600 s and 10 800 s due to the gradual decay of the random perturbations in the initial thermal field.

Not surprisingly, the increases in cellularity within the deeper cap clouds in this comparison are also associated with larger perturbation growth rates and smaller empirical e-folding times $(\tau_{buoy})_E$. These values are found from the curves in Fig. 9e, which show the growth in the maximum values of Δw within the updrafts labeled C_{shal}, $C_{control}$, and C_{deep} in Figs. 9a, 9c, and 9d, respectively, over the period $1000 \leq t \leq 1400$ s. Respective values of 736, 509, and 380 s are obtained for $(\tau_{buoy})_E$ in the IOP3-shal, IOP3-control, and IOP3-deep simulations, consistent with the linear model result that deeper clouds yield faster perturbation growth. The differences between $(\tau_{buoy})_L$ and $(\tau_{buoy})_E$, which are greatest in the IOP3-shal case (28%), and decrease successively in the IOP3-control (12%) and IOP3-deep (8%) cases, may be partly attributable to the vertical wind shear induced within the cloud by the mountain wave response. Because saturated regions reduce the effective stability of the flow, the mountain wave amplitude—and the forward shear it causes upstream of the barrier—depends on the depth of the cloudy layer, and is strongest for the shallow-cloud case. This increased shear is seen in Fig. 9c to cause a pronounced downwind tilt in the cellular perturbations for the IOP3-shal simulation, which is a departure from the upright structure assumed by (8) and, as discussed in section 4c, is associated with reductions in the growth rates of unstable perturbations.

These simulations with different cloud depths also demonstrate that the amount of cellular convection within orographic clouds is not uniquely determined by the profile of θ_e. Despite having nearly identical θ_e profiles
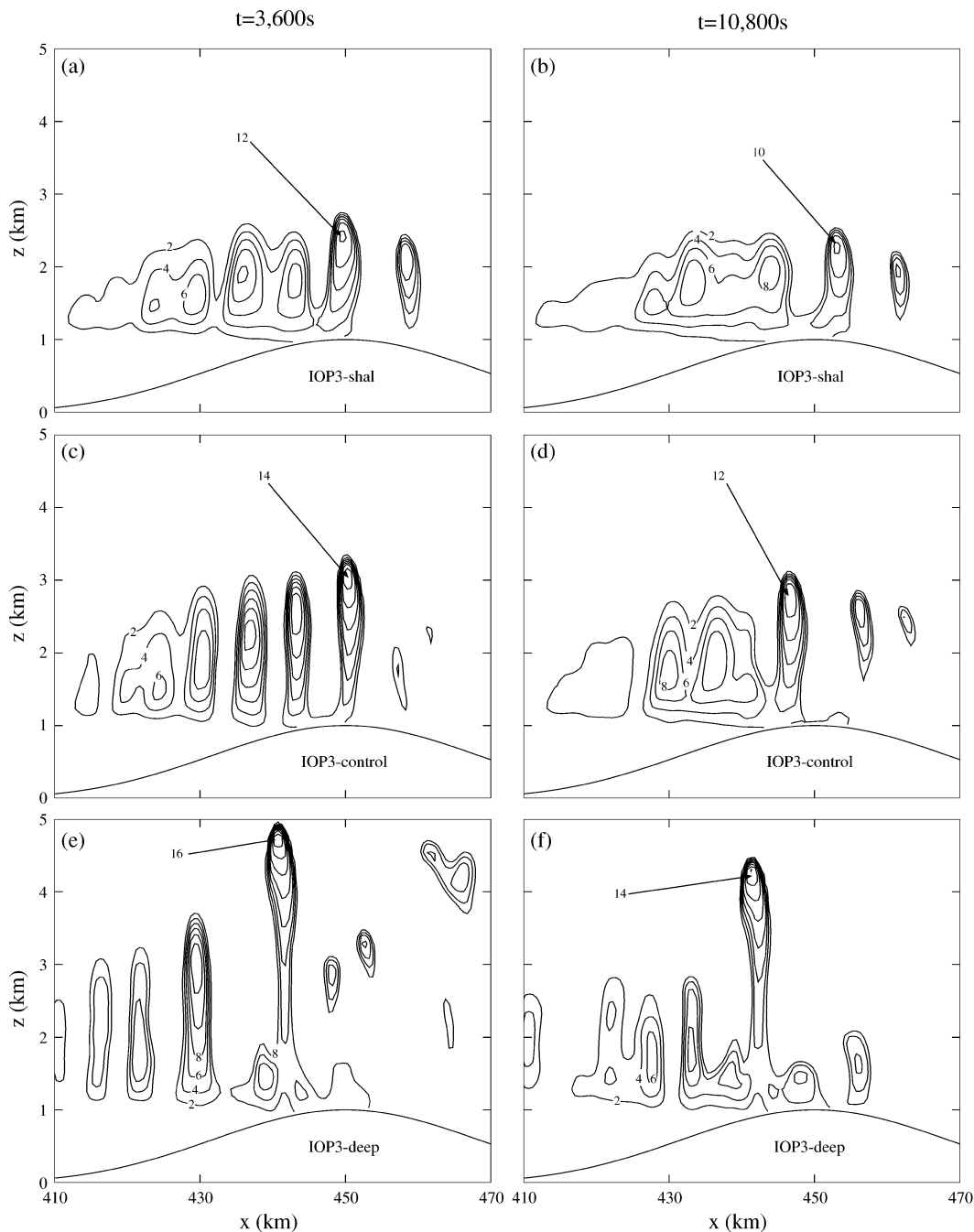
FIG. 12. Comparisons of q_c at $t = 3600$ and $10\,800$ s for simulations of varying cloud depth: (a) IOP3-shal at 3600 s, (b) IOP3-shal at 10 800 s, (c) IOP3-control at 3600 s, (d) IOP3-control at 10 800 s, (e) IOP3-deep at 3600 s, and (f) IOP3 deep at 10 800 s. Contour labels are multiplied by 10^{-4}.

throughout the layer $0 \leq z \leq 5$ km, large variations in cellularity are seen in the three simulations. The primary reason for this difference is due to the variation in the depth of the layer actually brought to saturation through orographic lifting. If the unstable layer (i.e., the saturated layer with negative N_m^2) is sufficiently shallow, the development of obvious convection within orographic clouds may be inhibited completely. The determination

of the minimum layer depth for cellularity, as well as the analysis of more complicated flows with multiple unstable layers, is, however, beyond the scope of this paper.

c. Wind shear

The presence of basic-state vertical wind shear has long been known to have a suppressive effect on con-

vection in planes parallel to the shear vector (e.g., Jeffreys 1928; Chandra 1938; Kuo 1963). A physical explanation for this phenomenon was provided by Asai (1964), who numerically solved the viscous 2D linear Boussinesq set of equations in the presence of positive vertical wind shear. Asai found that the downwind tilt of the convective axis induced by positive shear causes upward momentum transport, which reduces the strength of the convective perturbations by converting perturbation kinetic energy into that of the mean flow. In addition, the shear reduces the phase coherence between convective velocity and temperature perturbations, inhibiting the conversion of available potential energy into perturbation kinetic energy.

To quantify the effect of basic-state shear on the growth rate of convective perturbations in an unstable saturated shear flow, Hill (1968) obtained analytical solutions to (7) for flow in a channel with uniform static stability and a linear environmental shear profile. Hill found that the growth rate of unstable moist perturbations is substantially reduced in the presence of shear, particularly for deeper perturbations with small horizontal wavelengths. Based on these conclusions, it might be expected that vertical wind shear will generally tend to reduce the amount of cellular convection in 2D simulations. This hypothesis was tested by comparing a simulation with a piecewise-linear velocity profile,

$$U(z) = \begin{cases} 15 \ (\text{m s}^{-1}): & z < 1 \text{ km} \\ 15 + \dfrac{z - 1000}{2000} \ (\text{m s}^{-1}): & 1 \leq z \leq 4 \text{ km} \\ 30 \ (\text{m s}^{-1}): & z > 4 \text{ km,} \end{cases}$$
(13)

to the IOP3-control case for which U is constant at 15 m s^{-1} throughout the domain.

Because the presence of basic-state shear in the IOP3-shear simulation prevents the use of (12) for the estimation of τ_{buoy}, a quantitative comparison between the unstable perturbation growth rates calculated empirically and predicted from the two-layer linear model cannot be performed. Nonetheless, the suppression of cell growth in the IOP3-shear simulation can be seen in Fig. 7, which shows that the sheared case (Fig. 7d) produces a stratiform cloud with weak embedded convection rather than the fully cellular structure in the nonsheared IOP3-control simulation (Fig. 4a). From Table 1 it is also apparent that R_{max}, $(E_{\text{cloud}})_{\text{avg}}$, E_{flow}, and P_{avg} are all substantially reduced in the presence of environmental shear.

5. Moving from 2D to 3D

The inclusion of the third spatial dimension is necessary for realistic simulations of airflow over topography because this allows air to flow around, as well as over, an isolated mountain. In addition, it allows con-

vective circulations to develop around arbitrary axes of rotation. In particular, convective roll circulations may develop along the streamwise axis in 3D simulations, whereas such motions are precluded in the 2D framework.

a. Shear simulation with a quasi-2D ridge

To isolate the effects of three-dimensionality on the cellular structure of orographic clouds, two simulations are compared that have identical mountain profiles in the alongwind direction. The first (IOP3-shear) is the 2D simulation from section 4c, while the second simulation (IOP3-shear-q2D) involves a quasi-2D ridge with the same terrain profile in the x–z plane as the 2D case, and uniform topography in the y direction with periodic lateral boundaries at $y = 0$ and L_y. The flow cannot detour around the barrier in the IOP3-shear-q2D case, but circulations may still develop around arbitrary axes of rotation.

Profound differences between the 2D and 3D simulations are apparent in the q_c fields at 7200 s. At this time there are weak embedded cells in the 2D simulation (Fig. 7d), while longitudinal convective bands aligned with the basic-state wind vector have developed in the 3D case (Fig. 13a). These convective bands create localized areas with high q_c, thereby generating more intense precipitation. Table 1 shows that, in comparison to the 2D case, the 3D simulation produces a major increase in the value of R_{max}, and over a 10% higher $(E_{\text{cloud}})_{\text{avg}}$. In addition, E_{flow} and P_{avg} in the 3D simulation are nearly twice those for the 2D counterpart.

The roll-like character of the convective bands in Fig. 13a can be seen in Fig. 14, which shows the cloud-water field and the velocity vectors at 7200 s in a $y - z$ cross section at the mountain ridge crest ($x = 450$ km). Circulations around axes parallel to the mean wind vector (normal to the page) are clearly evident, with upward motion inside the clouds and downward motion outside. This circulation appears similar to that discussed by Asai (1970), in which streamwise rolls with rotational axes parallel to the environmental wind vector were the fastest-growing perturbations in linear stability analyses of dry statically unstable plane Couette flow.

b. Isolated ridge simulation

In the comparison of 2D and 3D parallel shear flows of the previous section, it was seen that the inclusion of a third spatial dimension allowed for the development of longitudinal convective circulations. Here we check the robustness of that result by performing a simulation (IOP3-shear-3D) that is otherwise identical to the IOP3-shear-q2D case except for the use of the more physically realistic isolated ridge topographic profile shown in Fig. 1. Note that the horizontal scale of the initial thermal perturbations in the IOP3-shear-3D case increases with the horizontal grid spacing on each of the coarser outer
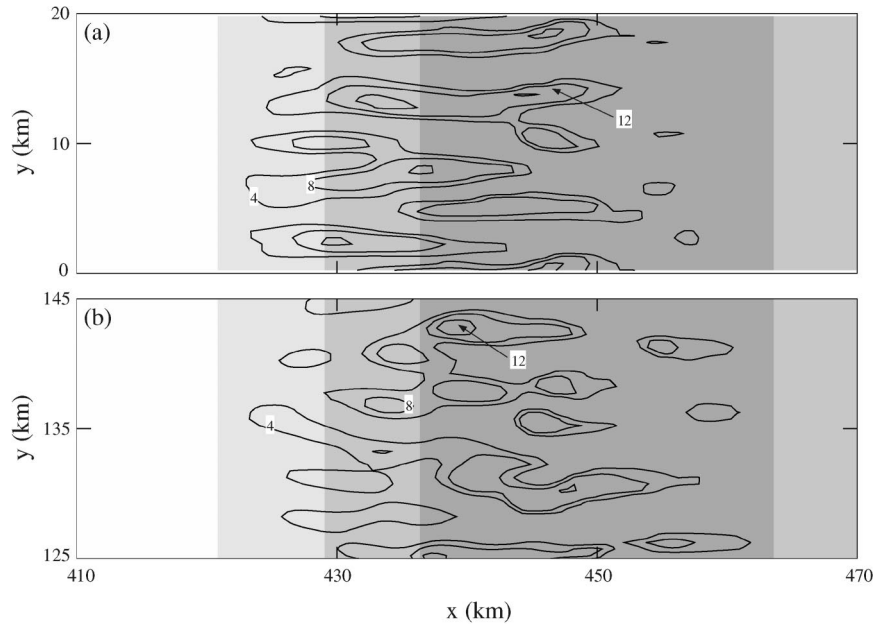
FIG. 13. Horizontal cross sections of q_c at $z = 2$ km in 3D simulations at $t = 7200$ s: (a) IOP3-shear-q2D simulation, (b) IOP3-shear-3D simulation. Contour labels are multiplied by 10^{-4}. Shaded contours indicate surface topography at 250-m intervals.

grids. Thus, to focus exclusively on the small-scale initial perturbations originating in the finest grid, which are the most effective at seeding convective motions, we terminate this fully 3D simulation at $t = 7200$ s, slightly before the lower-level air from the upstream end of the finest grid (at $x = 297$ km) is advected through the cloud.

A horizontal cross section of the q_c field of the IOP3-shear-q2D simulation at $z = 2$ km and $t = 7200$ s is compared to a similar cross section over the centermost 20 km of the IOP3-shear-3D simulation in Fig. 13. While both simulations produce convective bands oriented parallel to the flow, the bands in the uniform ridge case (Fig. 13a) are more elongated and well-organized than those in the isolated ridge case (Fig. 13b). This

difference is likely caused by the periodic y boundaries in the IOP3-shear-q2D simulation, which artifically favor the development of features parallel to the x direction. A series of simulations conducted with y periodic domains of different widths (not shown) have suggested that the regularity and character of the rolls in the quasi-2D case is not sensitive to the value of L_y.

Comparing the precipitation output of these two simulations over $0 \le t \le 7200$ s (note that, due to the shorter time interval, these values cannot be directly compared with those in Table 1), the values of $(E_{cloud})_{avg}$, E_{flow}, and P_{avg} are all slightly larger for the IOP3-shear-q2D simulation (68.1 mm h^{-1}, 38.7%, 2.6%, and 0.28 mm) than the IOP3-shear-3D simulation (50.2 mm h^{-1}, 35.6%, 1.8%, and 0.19 mm). This decrease in precipi-
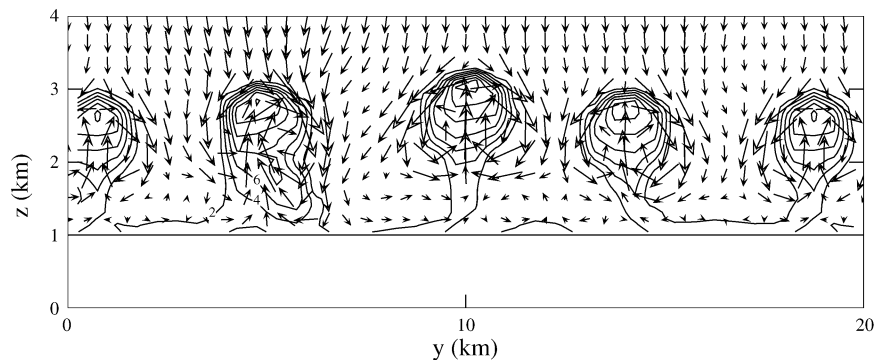

FIG. 14. Vertical cross section at $x = 450$ km of cloud liquid water and v, w velocity vectors for the IOP3-shear-q2D simulation at $t = 7200$ s; q_c field shown by solid contours, velocity vectors at each horizontal gridpoint and every third vertical gridpoint shown by arrows. Contour labels are multiplied by 10^{-4}.

tation intensity, efficiency, and accumulation for the IOP3-shear-3D case may be associated with the reduced low-level convergence upstream of the mountain caused by the flow detouring around the isolated barrier, resulting in a slightly shallower cloud whose leading edge is further downstream than that in the IOP3-shear-q2D case. As discussed in sections 4a and 4b, the effects of both the reduced cloud depth and reduced residence time tend to lessen the precipitation output from the orographic cloud.

6. Summary

The factors that govern the development of shallow cellular convection in warm orographic clouds have been investigated along with the effect of cellularity on orographic rainfall. Although potential instability, as determined by the sign of $d\theta_e/dz$ in an upstream sounding, generally serves as an adequate predictor of the development of a statically unstable environment within the cap cloud, the moist Brunt–Väisälä frequency provides a more accurate measure of the static stability of saturated layers. This is because the stability is not determined by the sign of $d\theta_e/dz$ alone. The numerical example presented in Fig. 5 confirmed that statically stable saturated layers may exist in which $d\theta_e/dz < 0$, but $N_m^2 > 0$.

The potential to develop negative N_m^2 through orographic lifting was shown to be only one of the factors that determine whether convection will actually develop in an orographic cloud. Other environmental and terrain-related factors that were seen to influence the development of cellularity in the numerical simulations of orographic clouds include 1) the mountain width and in-cloud residence time of the air parcels, 2) the depth of the unstable cap cloud, and 3) the environmental wind shear. Cellularity increases as the residence time of air parcels within the cloud increases—thus, wider mountains with broader cap clouds are more favorable for the generation of cells than narrow ridges. Deeper unstable regions within the cap cloud favor more rapid growth of the nascent cells. Finally, environmental wind shear suppresses the development of cells, at least in 2D.

In all cases, the simulations with more cellularity produced higher maximum rainfall rates and more average precipitation. Higher precipitation efficiencies were also obtained in the more cellular simulations, both with respect to the percentage of cloud water that was converted to surface rainfall (E_{cloud}) and the percentage of the water vapor impinging on the mountain that fell as precipitation (E_{flow}).

The preceding results, which were obtained from 2D simulations, are helpful for understanding the basic sensitivities of shallow orographic clouds to factors promoting cellularity. Nevertheless, the true 3D structure of embedded cellular convection in shallow orographic clouds can be quite different from that in the 2D simulations. The limited number of 3D simulations discussed in this study demonstrate that shallow convective structures may appear in 3D simulations of parallel shear flow when the corresponding 2D flow remains essentially stratiform, and that, in the 3D case, shallow convection tends to organize into roll-like convective bands oriented parallel to the basic-state wind vector. In comparison with the 2D case, the rolls in the 3D simulation generated more rain and higher precipitation efficiencies. The precise dynamics governing the convective rolls in the 3D simulations, such as the factors that control the roll intensity, orientation, and spacing, as well as the roll-induced momentum fluxes, is a focus of further research.

REFERENCES

Asai, T., 1964: Cumulus convection in the atmosphere with vertical wind shear: Numerical experiment. *J. Meteor. Soc. Japan,* **42,** 245–258.
——, 1970: Three-dimensional features of thermal convection in a plane couette flow. *J. Meteor. Soc. Japan,* **48,** 18–29.
Banta, R. M., 1990: *Atmospheric Processes over Complex Terrain. Meteor. Monogr.,* No. 45, Amer. Meteor. Soc., 323 pp.
Bougeault, P., and Coauthors, 2001: The MAP special observing period. *Bull. Amer. Meteor. Soc.,* **82,** 433–462.
Browning, K. A., F. F. Hill, and C. W. Pardoe, 1974: Structure and mechanism of precipitation and the effect of orography in a wintertime warm sector. *Quart. J. Roy. Meteor. Soc.,* **100,** 309–330.
Bryan, G. H., and J. M. Fritsch, 2000: Moist absolute instability: The sixth static stability state. *Bull. Amer. Meteor. Soc.,* **81,** 1207–1230.
Caraceña, F., R. A. Maddox, L. R. Hoxit, and C. F. Chappell, 1979: Mesoanalysis of the Big Thompson storm. *Mon. Wea. Rev.,* **107,** 1–17.
Chandra, K., 1938: Stability of fluids heated from below. *Proc. Roy. Soc. London,* **164A,** 231–242.
Chu, C.-M., and Y.-L. Lin, 2000: Effects of orography on the generation and propagation of mesoscale convective systems in a two-dimensional conditionally unstable flow. *J. Atmos. Sci.,* **57,** 3817–3837.
Dirks, R. A., 1973: The precipitation efficiency of orographic clouds. *J. Rech. Atmos.,* **7,** 177–184.
Douglas, C. K. M., and J. Glasspoole, 1947: Meteorological conditions in heavy orographic rainfall. *Quart. J. Roy. Meteor. Soc.,* **73,** 11–38.
Durran, D. R., and J. B. Klemp, 1982: On the effects of moisture on the Brunt-Väisälä frequency. *J. Atmos. Sci.,* **39,** 2152–2158.
——, and ——, 1983: A compressible model for the simulation of moist mountain waves. *Mon. Wea. Rev.,* **111,** 2341–2361.
Elliott, R. D., and E. L. Hovind, 1964: The water balance of orographic clouds. *J. Appl. Meteor.,* **3,** 235–239.
Emanuel, K. A., 1994: *Atmospheric Convection.* Oxford University Press, 580 pp.
Epifanio, C. C., and D. R. Durran, 2001: Three-dimensional effects in high-drag-state flows over long ridges. *J. Atmos. Sci.,* **58,** 1051–1065.
Fraser, A. B., R. C. Easter, and P. V. Hobbs, 1973: A theoretical study of the flow of air and fallout of solid precipitation over mountainous terrain. Part I: Airflow model. *J. Atmos. Sci.,* **30,** 801–812.
Glickman, T. S., Ed., 2000: *Glossary of Meteorology.* 2d ed. Amer. Meteor. Soc., 850 pp.

Grossman, R. L., and D. R. Durran, 1984: Interaction of low-level flow with the western Ghat Mountains and offshore convection in the summer monsoon. *Mon. Wea. Rev.,* **112,** 652–672.

Hill, G. E., 1968: On the orientation of cloud bands. *Tellus,* **20,** 132–137.

Hobbs, P. V., R. C. Easter, and A. B. Fraser, 1973: A theoretical study of the flow of air and fallout of solid precipitation over mountainous terrain. Part II: Microphysics. *J. Atmos. Sci.,* **30,** 813–823.

Houze, R. A., 2001: Orographic control of precipitation: What are we learning from MAP? *Mesoscale Alpine Programme Newsl.,* **14,** 3–15.

Jeffreys, H., 1928: Some cases of instability in fluid motion. *Proc. Roy. Soc. London,* **118A,** 195–208.

Kuo, H. L., 1963: Perturbations of plane couette flow in stratified fluid and origin of cloud streets. *Phys. Fluids,* **6,** 195–211.

Lalas, D. P., and F. Einaudi, 1974: On the correct use of the wet adiabatic lapse rate in the stability criteria of a saturated atmosphere. *J. Appl. Meteor.,* **13,** 318–324.

LeVeque, R. J., 1996: High-resolution conservative algorithms for advection in incompressible flow. *SIAM J. Numer. Anal.,* **33,** 627–665.

Lilly, D. K., 1962: On the numerical simulation of buoyant convection. *Tellus,* **14,** 148–172.

Parsons, E. B., and P. V. Hobbs, 1983: The mesoscale and microscale structure and organization of clouds and precipitation in midlatitude cyclones. IX: Some effects of orography on rainbands. *J. Atmos. Sci.,* **40,** 1930–1949.

Rogers, R. R., and M. K. Yau, 1989: *A Short Course in Cloud Physics.* Butterworth-Heineman, 290 pp.

Smith, R. B., 1982: A differential model of thermal advection. *Mon. Wea. Rev.,* **110,** 306–309.